*J. Fluid Mech.* (2025), *vol.* 1020, A15, doi:10.1017/jfm.2025.10603

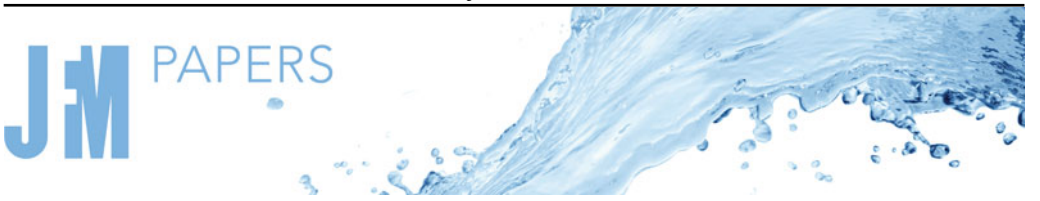


# Dynamics of bubble collision and coalescence in three-dimensional turbulent flows

**Shiyong Tan**[1], **Shijie Zhong**[1], **Yinghe Qi**[1], **Xu Xu**[1] **and Rui Ni**[1]

[1]Department of Mechanical Engineering, Johns Hopkins University, 3400 N. Charles St., Baltimore, MD 21218, USA

**Corresponding author:** Rui Ni, rui.ni@jhu.edu

(Received 15 November 2024; revised 4 July 2025; accepted 12 August 2025)

Turbulence exhibits a striking duality: it drives concentrated substances apart, enhancing mixing and transport, while simultaneously drawing particles and bubbles into collisions. Little experimental data exist to clarify the latter process due to challenges in techniques for resolving bubble pairs from afar to coalescence via turbulent entrainment, film drainage and rupture. In this work, we tracked pairs of bubbles across nearly four orders of magnitude in spatial resolution, capturing the entire dynamics of collision and coalescence. The resulting statistics show that critical variables exhibit scalings with bubble size in ways that are different from some classical models, which were developed based on assumptions that bubble collision and coalescence only mirror the key scales of the surrounding turbulence. Furthermore, contrary to classical models which suggest that coalescence favours slow collision velocity, we find a 'Goldilocks zone' of relative velocities for bubble coalescence, where there is an optimal coalescence velocity that is neither too high nor too low. This zone arises from the competition between bubble–bubble and bubble–eddy interactions. Incorporating this zone into the new model yields excellent agreement with experimental results, laying a foundation for better predictions for many multiphase flow systems.

**Key words:** breakup/coalescence

## 1. Introduction

Turbulence accelerates two seemingly contradictory processes: dispersing particles orders of magnitude faster than pure molecular diffusion (Toschi & Bodenschatz 2009; Tan & Ni 2022; Shnapp *et al.* 2023; Huang *et al.* 2025) and also drawing bubbles and particles together (Pumir & Wilkinson 2016). The latter plays a crucial role in applications where turbulence fosters the growth of flocculated particles in wastewater treatment (Zhao *et al.*

© The Author(s), 2025. Published by Cambridge University Press. This is an Open Access article, distributed under the terms of the Creative Commons Attribution licence (https://creativecommons.org/licenses/by/4.0/), which permits unrestricted re-use, distribution and reproduction, provided the original article is properly cited.



https://doi.org/10.1017/jfm.2025.10603 Published online by Cambridge University Press

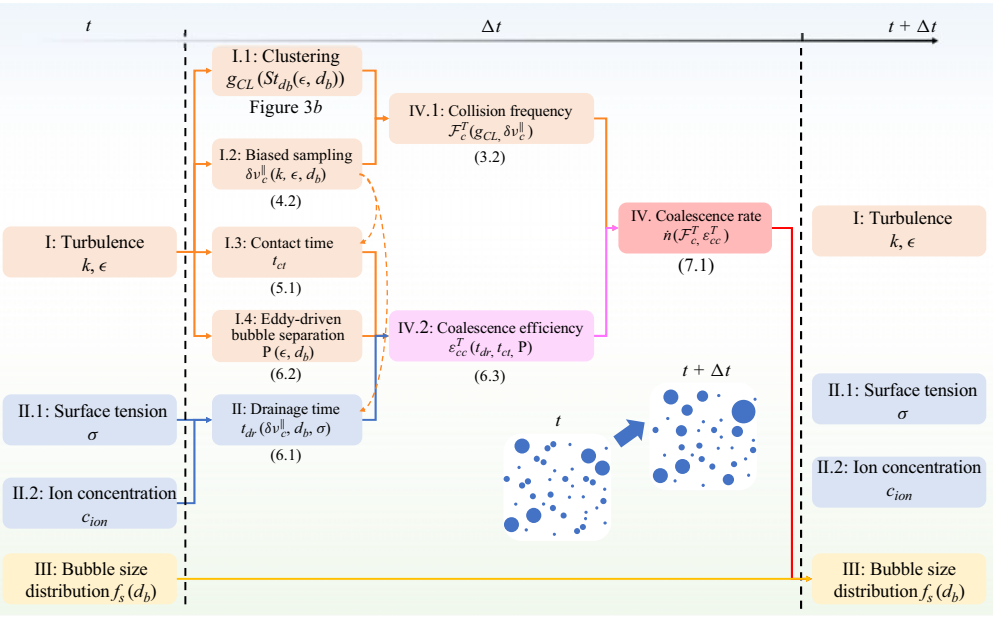


Figure 1. Flow chart of a pseudo-code with key steps and their associated equation number to compute bubble size evolution due to coalescence from $t$ to $t + \Delta t$.

2021) and microbubbles in chemical and nuclear reactors (Liao & Lucas 2010; Lohse 2018; Mathai, Lohse & Sun 2020; Ma *et al.* 2025). However, the impact of turbulence on the bubble collision and coalescence dynamics remains a mystery. This enigma persists due to the vast spectrum of processes involved, spanning over eight orders of magnitude in separations. This range encompasses the dispersion of microbubbles over centimetre distances (Mathai *et al.* 2018), collisions occurring at millimetre scales (Prince & Blanch 1990*a*; Wu *et al.* 1998; Lehr, Millies & Mewes 2002; Wang, Wang & Jin 2005) and the subsequent film drainage and microscopic connecting liquid bridge at micrometre dimensions (Paulsen *et al.* 2014; Bartlett *et al.* 2023; Ozan, Solsvik & Jakobsen 2023).

The coalescence rate $\dot{n}$, one of key quantities in the population balance equation (Williams 1985) in addition to the bubble breakup rate (Ni 2024; Vela-Martín & Avila 2022; Qi *et al.* 2022, 2024), plays a significant role in the prediction of the evolution of the bubble size distribution. The governing parameters affecting bubble coalescence in turbulence are illustrated in the flowchart in figure 1, which illustrates the procedure to compute the bubble size distribution from time $t$ to $t + \Delta t$ driven by the coalescence. The breakup process needs to be computed separately. The procedure follows the classical formulation, where the coalescence rate is determined by the collision frequency (IV.1 in figure 1) and coalescence efficiency (IV.2).

A widely used model for the bubble coalescence rate shows $\dot{n} = \mathcal{F}_c \cdot \mathcal{E}_{cc}$, in which $\mathcal{F}_c$ describes how frequently two bubbles collide (IV.1 in figure 1) and $\mathcal{E}_{cc}$ determines how often those collisions result in coalescence (IV.2 in figure 1). Based on the kinetic gas theory of Kennard *et al.* (1938), the collision frequency $\mathcal{F}_c$ can be modelled as $\mathcal{F}_c = nS\delta v$, where $n$ is the bubble number density, $S$ is the cross-sectional area of the circumcircle of both bubbles and $\delta v$ is the relative velocity between the two bubbles during a collision, which can also be called the collision or approach velocity (Liao & Lucas 2010). Coulaloglou & Tavlarides (1977) assumed that the approach velocity should be the velocity of the eddies of the bubble size. For collision of two equally sized bubbles



https://doi.org/10.1017/jfm.2025.10603 Published online by Cambridge University Press

with diameter $d_b$, the collision velocity can be readily formulated through the Kolmogorov theory as $\delta v = C_2 \epsilon^{1/3} d_b^{1/3}$, where $C_2$ is a constant and $\epsilon$ is the dissipation rate. Although this framework has been widely adopted (Lee, Erickson & Glasgow 1987; Prince & Blanch 1990*a*; Luo 1995), no experimental observation is available to substantiate this key hypothesis so far.

Regarding the coalescence efficiency, a widely accepted concept introduced by Ross (1971) and Coulaloglou (1975) suggests that the probability of coalescence (IV.2 in figure 1) depends on the contact time between two colliding bubbles, which is formulated as $\mathcal{E}_{cc} = \exp(-t_{dr}/t_{ct})$, where $t_{dr}$ is the drainage time required for the film to thin down to a critical thickness (II in figure 1), and $t_{ct}$ is the duration that two bubbles remain in close proximity (I.3 in figure 1). Nevertheless, determining the contact time between bubbles in turbulent flows poses significant theoretical challenges due to the complex and evolving nature of film drainage processes (Chesters & Hofman 1982; Chen, Hahn & Slattery 1984; Oolman & Blanch 1986; Jeelani & Hartland 1998; Danov, Valkovska & Ivanov 1999; Chesters & Bazhlekov 2000; Lu *et al.* 2019; Prince & Blanch 1990*b*; Firouzi, Howes & Nguyen 2015), compounded by the chaotic nature of turbulence. The earliest estimation of the contact time relies on dimensional analysis, similar to the turnover time of an equal-sized eddy, $t_{ct} \propto d_b^{2/3}/\epsilon^{1/3}$. Later, several refined models were developed, which also present a similar scaling with $d_b$, either through analysing the energy balance between kinetic energy and surface energy (Chesters 1991), or by deriving the interaction time based on the parallel film model (Luo 1995; Kamp *et al.* 2001).

Several recent studies suggest that collision and coalescence cannot be treated independently (Das 2015; Gong *et al.* 2020; Ozan *et al.* 2021, 2023), based on the fact that they both depend on the approach velocity (Doubliez 1991; Duineveld 1996; Lehr & Mewes 2001; Lehr *et al.* 2002). As a result, the coalescence rate can be formulated as $\dot{n} = \int S \delta v \mathcal{E}_{cc}(d_b, \delta v) f_v^c(\delta v) \mathrm{d}\delta v$, where $f_v^c(\delta v)$ is the probability distribution function of the approach velocity $\delta v$. The coalescence probability $\mathcal{E}_{cc}(d_b, \delta v)$ is obtained either from analytical derivation based on an energy balance during collision (Kamp *et al.* 2001; Das 2015) or from simulations of film drainage (Gong *et al.* 2020; Ozan, Hosen & Jakobsen 2021).

Many models developed for bubble collision and coalescence, although with some variations, shared many similar hypotheses on the collision velocity, contact time and coalescence efficiency, none of which has been measured in three-dimensional (3-D) turbulence. In this work, we employed an advanced in-house 3-D bubble-tracking algorithm (Tan *et al.* 2023*b*) that can effectively track dense bubbles in 3-D turbulent environments. By accurately capturing all critical parameters that were unavailable before, we develop a new model that accounts for the effect of bubble–turbulence interactions during bubble collision and coalescence. This model integrates additional effects identified in our study, including clustering (I.1), biased sampling (I.2) and eddy-driven bubble separation (I.4), which are introduced in the following sections. In addition, the key variables such as $\mathcal{F}_c$ and $\mathcal{E}_{cc}$ are denoted with a superscript $T$ to emphasise that they are different in turbulent flows whose effects will be measured and modelled in this work. To place our findings in context, we compare them with the classical model of coalescence efficiency, originally developed by Ross (1971), Coulaloglou (1975) and Chesters (1975), hereafter referred to as the RCC model.

## 2. Three-dimensional bubble tracking at high image densities

Bubble collision and coalescence can be affected by both turbulence and buoyancy. To simplify the problem and focus on the turbulence effect, we constructed a unique setup



https://doi.org/10.1017/jfm.2025.10603 Published online by Cambridge University Press

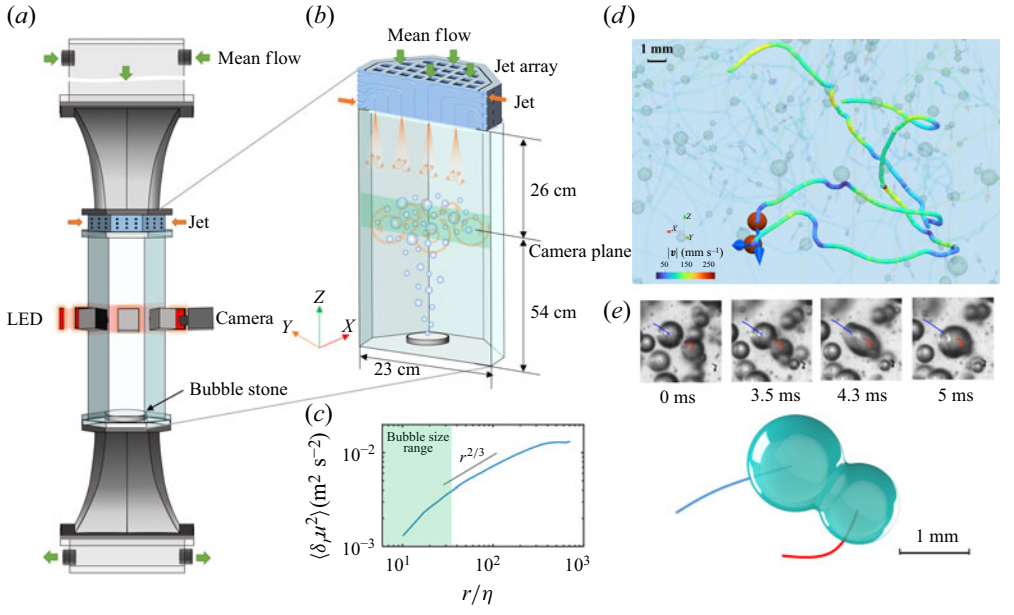


Figure 2. Experimental facility and 3-D Lagrangian bubble tracking. (*a*) Schematic of the experimental set-up, (*b*) schematic of the test section including the jet array and the bubble generator, (*c*) the second-order longitudinal structure function of turbulence in the test section, (*d*) trajectories of a colliding bubble pair coloured by velocity magnitude in the presence of background bubbles tracked at the same time and (*e*) consecutive bubble images before and after the moment of coalescence along with the 3-D reconstruction of the two bubbles and the merging interface in between.

that features intense turbulence, as depicted in figures 2(*a*) and 2(*b*), known as V-ONSET (Masuk *et al.* 2019*b*; Tan *et al.* 2023*a*). The jet array injects powerful jets, producing turbulence with a high Taylor Reynolds number, $Re_\lambda = u'\lambda/\nu = 493$, where $u'$ is the root-mean-squared fluctuation velocity, the Taylor microscale $\lambda$ is $\sqrt{15\nu/\epsilon}u'$ and $\nu$ is the kinematic viscosity of the fluid, enabling a wide scale separation from the Kolmogorov scale $\eta$ of 0.07 mm to the integral scale $L$ of 110 mm. The turbulent kinetic energy is $k = 0.29\,\mathrm{m^2\,s^{-2}}$. Figure 2(*c*) illustrates the second-order longitudinal structure function, $D_{LL}(r)$, which displays a distinct scaling law of $r^{2/3}$, aligning with the well-established Kolmogorov theory for fully developed turbulence (Kolmogorov 1949). The turbulence energy dissipation rate estimated from the structure function is $0.03\,\mathrm{m^2\,s^{-3}}$ and the Taylor microscale is calculated to be 2.9 mm. Bubbles were produced by an ultra-fine bubble generator at the bottom of the octagonal test section. The bubble size distribution is presented in figure 3(*a*) and the diameter ranges from 0.2 to 2 mm ($3\eta$–$30\eta$). The rise velocity for bubbles in this range is approximately $0.1\,\mathrm{m\,s^{-1}}$ (Salibindla *et al.* 2020), and its ratio to $u'$ is around 1, yielding a bubble Reynolds number of the order of 100. The void fraction, $\alpha$, in our experiments is approximately 0.04 %. The detailed setup parameters and flow control specifications are provided in Appendix A.

At the moderate Reynolds number, the Strouhal number, *Str*, is approximately 0.18, leading to a vortex shedding time scale of $\tau_f = d_b/(v_b Str) \approx 55$ ms. In comparison, the eddy turnover time at the same length scale can be estimated as $\tau_{d_b} = d_b^{2/3}/\epsilon^{1/3} \approx 3.2$ ms, which is an order of magnitude smaller than the bubble vortex shedding time scale. This suggests that the wake structures generated by the bubbles are rapidly convected by the surrounding turbulent eddies, and the bubble motion is mostly governed by the turbulence.



https://doi.org/10.1017/jfm.2025.10603 Published online by Cambridge University Press

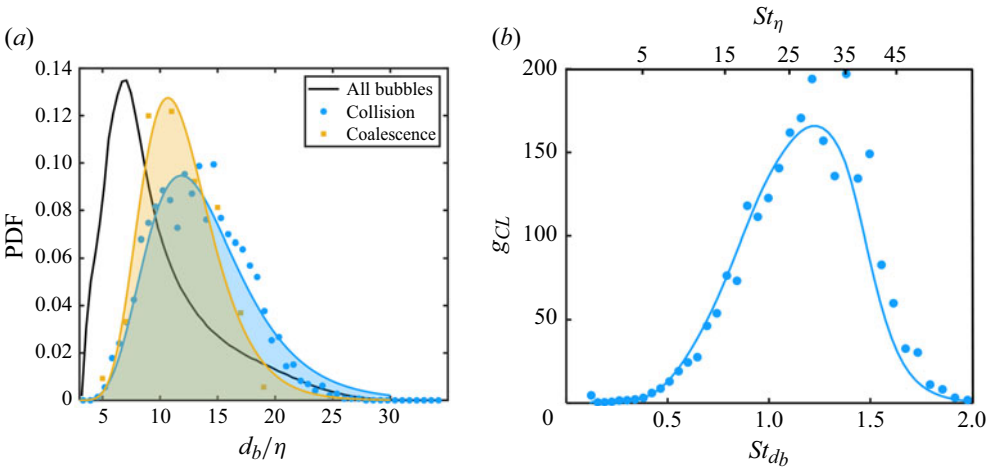


Figure 3. (*a*) Bubble size distribution for all bubbles, and only those in collision and coalescence events. The shaded probability density function (PDF) is fitted with a log-normal distribution function for better illustration. (*b*) The collision kernel representing the clustering effect as a function of two Stokes numbers based on two different time scales, the $St_\eta$ Kolmogorov scale and $St_{d_b}$ based on the bubble-sized eddies.

Furthermore, the rate of potential energy injection to turbulence by bubble buoyancy, given by $\alpha g w_b$ (where $w_b$ is the bubble rise velocity), is estimated to be approximately $0.0003\ \mathrm{m^2\,s^{-3}}$ as the void fraction $\alpha \approx 0.04\,\%$ is very small. In comparison, the energy dissipation rate is $0.03\ \mathrm{m^2\,s^{-3}}$, much larger than the buoyancy effect, suggesting the modulation by bubbles to turbulent background flows is negligible.

Four cameras positioned at the periphery of the test section, as illustrated in figure 2(*a*), are used to capture the bubble motion. As the bubble concentration increases to acquire sufficient collision and coalescence events, the occurrence of overlapping bubble images increases, leading to challenges in tracking bubbles pairs in close proximity (Katz & Sheng 2010; Xue, Qu & Wu 2013; Lebon *et al.* 2016; Mathai *et al.* 2018; Masuk *et al.* 2019*a*; Salibindla *et al.* 2020; Shao *et al.* 2020; Song *et al.* 2022; Wu *et al.* 2020). To address this challenge, a new method is developed to utilise temporal information (bubble images may not overlap prior to the moment when they do) to predict the bubble location and then cross-correlated the predicted images against the captured ones to identify the most probable location of the bubble (a brief overview of this new method is provided in Appendix B). The tracked bubble locations correspond to the centroids of the bubbles, as those within the specified size range are spherical. Velocity and acceleration are determined by convolving the position data with a Gaussian kernel (Mordant, Crawford & Bodenschatz 2004; Ni, Huang & Xia 2012) to eliminate noise.

By applying this method, we were able to track bubbles with high image densities with up to 87 % of the area overlapped with neighbours (Tan *et al.* 2023*b*). Figure 2(*d*) shows trajectories, coloured by velocity magnitude, of a sample pair of bubbles that collide with each other, in the presence of a high concentration of background bubbles. The time series of the coalescence moment is shown in figure 2(*e*). The reconstructed position of bubbles can achieve a high level of precision at around 10 μm, reaching sub-pixel accuracy through the utilisation of bilinear interpolation (Press *et al.* 2007) in close proximity to the peak of the image cross-correlation. This technique allows us to determine the bubble pairs when they are as close as 20 μm, even allowing for 3-D reconstruction of the merging interface, as shown in figure 2(*e*). So the separation that can be resolved is close to four orders of magnitude from 20 μm to 5 cm.



https://doi.org/10.1017/jfm.2025.10603 Published online by Cambridge University Press

From the experimental images of bubble motion, we identified around $3.85 \times 10^6$ individual bubbles and their corresponding trajectories. Any two bubbles appearing simultaneously within the view volume were considered a potential bubble pair, resulting in approximately $7 \times 10^8$ pairs in our datasets, which is sufficient for calculating the bubble structure function and approach velocity of collision, as detailed in the following section.

## 3. Size distribution and size ratio

The bubble size distribution, computed from $3.85 \times 10^6$ tracked bubbles, is presented as a black solid line in figure 3(*a*), spanning from $3\eta$ to $30\eta$ with a peak located at $7\eta$. Based on the trajectories of these bubbles, collision events were identified when the film thickness between two bubbles, $|r - d_b|$, fell below $0.2d_b$ (Gong *et al.* 2020). Finally, only those events when the film thickness was below 10 µm were checked manually against experimental images to identify bubble pairs that ultimately coalesce.

The representative size of bubble pairs involved in bubble collisions and coalescence is characterised by the equivalent bubble diameter, defined as $d_{eq} = 2d_{b1}d_{b2}/(d_{b1} + d_{b2})$. As we will show later, the collision and coalescence are dominated by events with two similar-sized bubbles. For simplicity, $d_b$ is used in place of $d_{eq}$ wherever $d_{eq}$ is intended. The size distribution of $d_b$ of bubble pairs undergoing collision events is shown in figure 3(*a*) as blue dots. The blue curve with the shaded area represents the log-normal fit to the PDF. It is evident that the PDF for collision events peaks at a larger size compared with the overall bubble distribution. This shift may be attributed to preferential concentration, where bubbles of certain sizes tend to cluster due to inertial effects, leading to locally elevated concentrations in turbulence – especially in the intermediate Stokes number range (Rensen, Luther & Lohse 2005; Calzavarini *et al.* 2008). To quantify this clustering behaviour, we introduce a size-dependent clustering function $g_{CL}(d_b)$, which describes how the likelihood of collisions between bubbles of diameter $d_b$ deviates from what would be expected under a random, uniform distribution. Specifically, we relate the measured size distribution of collided bubble pairs, $f_d^c(d_b)$, to the overall bubble size distribution $f_d(d_b)$ via

$$f_d^c(d_b) = \frac{f_d^2(d_b)\, g_{CL}(d_b)}{\int_0^\infty f_d^2(d_b)\, g_{CL}(d_b)\, \mathrm{d}d_b}. \tag{3.1}$$

Here, $f_d^2(d_b)$ is the expected distribution of randomly selected bubble pairs, and $g_{CL}(d_b)$ accounts for the enhanced probability of collisions due to clustering. From (3.1), $g_{CL}(d_b)$ can be directly computed using the measured distributions $f_d(d_b)$ (black solid line) and $f_d^c(d_b)$ (blue) shown in figure 3(*a*). The resulting values are plotted as blue dots in figure 3(*b*). In addition, the blue solid line represents a smoothed curve of $g_{CL}$ by using the fitted PDF of collision events. Since the Stokes number is widely used in the analysis of the clustering effect (Loth 2000), the $x$-axis is presented in terms of the Stokes number, $St = d_b^2/36\nu\tau_{fb}$, where $\tau_{fb}$ represents the characteristic time scale of the flows around bubbles. There are two possible time scales for $\tau_f$, the Kolmogorov time scale, $\tau_\eta = (\nu/\epsilon)^{1/2}$, which is used in the study by Mathai *et al.* (2016) for micro-bubbles, and the bubble-sized eddy turnover time, $\tau_{d_b} = d_b^{2/3}/\epsilon^{1/3}$. The Stokes numbers based on both flow time scales, $St_\eta$ and $St_{d_b}$, are also shown as the top and bottom $x$-axes in figure 3(*b*), respectively.

Interestingly, instead of $St_\eta$, the curve of $g_{CL}(St_{d_b})$ exhibits a peak near $St_{d_b} = 1$, which suggests that $St_{d_b}$ is more appropriate to characterise the preferential concentration effect



https://doi.org/10.1017/jfm.2025.10603 Published online by Cambridge University Press

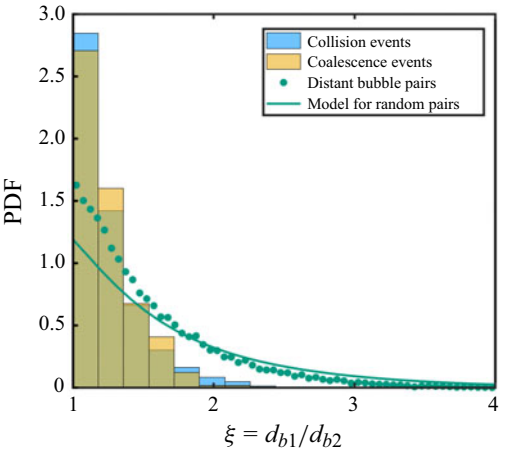


Figure 4. The PDF of the bubble size ratio $\xi$ for bubble pairs with sizes $d_{b1}$ and $d_{b2}$, respectively, in collision and coalescence events, as well as distant bubble pairs.

of bubbles in turbulence. The dimensionless function $g_{CL}(St_{d_b})$ expressed in terms of $St_{d_b}$ should be applicable to other bubbly flows, provided that bubble–turbulence modulation remains negligible, as discussed in § 2.

By using $g_{CL}$, the bubble collision frequency in turbulence can be estimated as follows:

$$\mathcal{F}_c^T(d_b) = n^2 f_d^c(d_b)\mathrm{d}d_b \pi d_b^2 \delta v_c^{\parallel}(d_b), \tag{3.2}$$

where $n$ is the number density of all bubbles in the flows. The parameter $f_d^c(d_b)\mathrm{d}d_b$ represents the probability of colliding bubble pairs with size $d_b \pm \mathrm{d}d_b$, and $f_d^c(d_b)$ is obtained through (3.1) in terms of $g_{CL}$ and $f_d(d_b)$.

The PDF for coalescence is also shown as yellow symbols in figure 3(*a*), which is considerably narrower than that for collision events, indicating that the efficiency of coalescence is probably also size dependent. It will be further examined in § 6.

In addition to the size distribution, since collision and coalescence may occur between bubble pairs of different sizes, the size ratio, defined as $\xi = d_{b1}/d_{b2}$, was also computed. The resulting distributions are shown as blue and yellow histograms in figure 4. It is evident that both collision and coalescence are dominated by similar-sized pairs. To ensure that this is not a result of the size distribution alone, a PDF of bubble pairs that are at $80\eta$ away is shown as green dots, which shows a flatter distribution, indicating more uneven sized pairs. At this far distance, the dynamics of the bubbles becomes less correlated and the distribution becomes almost random. If we assume the bubble locations are completely random, the probability of finding a pair with a certain size ratio based solely on the bubble size distribution, is represented by the green solid line in figure 4, which is close, although not perfect, to the experimental measurement, suggesting that these pairs are close to random at large enough separations.

The bias of the PDF for collisions from that of distant bubble pairs is likely due to the preferential concentration effect in turbulence, where bubbles of similar sizes tend to cluster within eddies of similar size, increasing their likelihood of collision. The distribution for coalescence events (yellow histogram) closely follows that of collisions but is slightly more constrained, suggesting that coalescence is even more probable when the size ratio is closer to unity.



https://doi.org/10.1017/jfm.2025.10603 Published online by Cambridge University Press

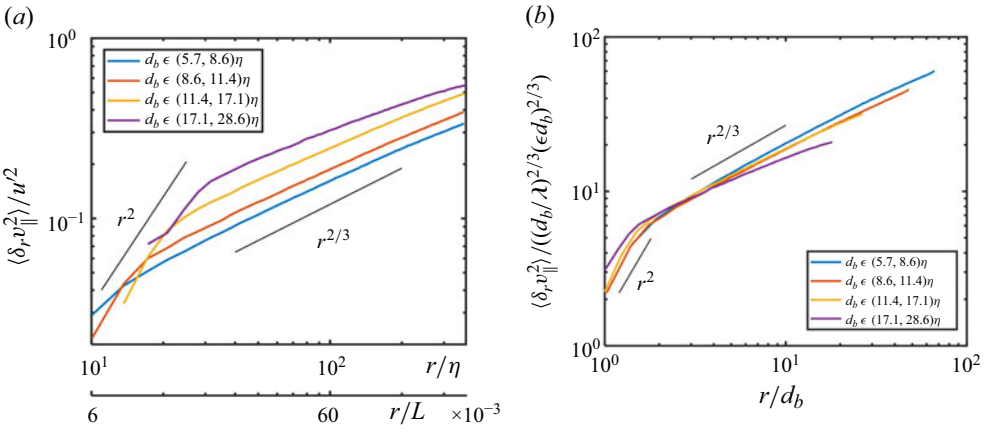


Figure 5. The second-order longitudinal bubble velocity structure function between bubbles with similar size, normalised ($a$) with the turbulent fluctuation velocity $u'$ and ($b$) with bubble-scaled kinematic energy $(d_b/\lambda)^{2/3}(\epsilon d_b)^{2/3}$, versus the bubble separation normalised ($a$) with the Kolmogorov scale and the integral length scale and ($b$) with the bubble diameter.

To be more quantitative, 98 % of collision events occur within $\xi < 2$. Consequently, in the subsequent analysis, the discussion focuses on the collision and coalescence of bubble pairs with common size.

## 4. Bubble structure function and bubble approach velocity

For $7 \times 10^8$ bubble pairs, we project their velocity differences in the direction of their separation, $\delta_r v^{\parallel}(r) = v_{\parallel}(\boldsymbol{x} + \boldsymbol{r}) - v_{\parallel}(\boldsymbol{x})$. The collision velocity is defined as $\delta_r v^{\parallel}(r)$ at $r = 1.2d_b$, which is the separation when the film between two bubbles starts to be drained (Gong *et al.* 2020). Nevertheless, to fully understand the entire bubble dynamics, in this section, we extend the relative velocity to a wide range of separations, which is similar to the structure function studied in single-phase turbulence.

The second-order bubble structure function is defined as $D_{LL}^B(r) \equiv \langle \delta_r v_\parallel^2 \rangle$. The measured bubble structure functions are presented in figure 5($a$). Bubbles are divided into four groups based on their size. Each curve in figure 5($a$) represents the statistics of bubble pairs in the same bubble group.

Two distinct scalings can be observed. When two bubbles are sufficiently far apart, $r > 2d_b$, the structure function $D_{LL}^B$ follows $r^{2/3}$, similar to the inertial-range scaling observed in single-phase turbulence. This similarity arises because the motion between bubbles with a large separation is predominantly influenced by large-scale turbulent transport. As the separation between bubbles decreases below $2d_b$, $D_{LL}^B$, transitions to a scaling of 2. Unlike the Kolmogorov scale $\eta$, which marks the transition between the dissipative and inertial ranges, the bubble structure function transitions between two scalings at $2d_b$. This transition scaling with bubble size suggests that the $r^2$ scaling is not due to the turbulence's dissipative range but rather to the linear dependence of the bubble relative velocity on separation. A plausible explanation for this linear dependence is the entrainment of bubble pairs by a common vortex, causing their relative acceleration to scale as $\delta a \sim r$. The value of $\delta a$ can be expressed in terms of $\delta v$ as $\delta a = \delta v \mathrm{d}\delta v/\mathrm{d}r$, which finally leads to $\delta v^2 \sim r^2$.

More importantly, a noticeable observation is the upward shift of the curves as the bubble size increases, despite the fact that the structure functions are normalised by



https://doi.org/10.1017/jfm.2025.10603 Published online by Cambridge University Press

turbulence scales, which indicates that the bubble dynamics does not simply mirror that of the surrounding eddies, as incorrectly assumed in many models. The key missing piece is the biased sampling, i.e. bubbles preferentially get entrained in eddies of similar sizes (Wang *et al.* 2024). Subsequently, by further non-dimensionalising $D_{LL}^{B}$ with the eddy energy that scales as $(d_b/\lambda)^{2/3}$, we obtain the normalised plot presented in figure 5(*b*). The curves exhibit a reasonable collapse in both limits, i.e. $r^2$ and $r^{2/3}$, providing support to the biased sampling argument. By utilising the collapse observed in figure 5(*b*), we can readily formulate the bubble structure function as follows:

$$D_{LL}^{B}(r, d_b) = \begin{cases} C_0(d_b/\lambda)^{2/3}(\epsilon d_b)^{2/3}(r/d_b)^2 & \text{for } r \leqslant 2d_b, \\ C_1(d_b/\lambda)^{2/3}(\epsilon d_b)^{2/3}(r/d_b)^{2/3} & \text{for } 2d_b < r \ll L, \end{cases} \tag{4.1}$$

where $C_0$ and $C_1$ are constants. From the data plotted in figure 5, $C_0$ and $C_1$ are estimated to be 1.73 and 4.36, respectively, both of which are the order of unity, suggesting that the additional term of biased sampling is reasonable.

Equation (4.1) readily provides the estimation of the approach velocity which is defined as the relative bubble velocity before the lubrication pressure slows them down, which begins at around $r = 1.2d_b$ (Gong *et al.* 2020). The approach velocity, $\delta v_c^{\parallel}$, can then be determined by setting $r = 1.2d_b$ in the bubble structure function

$$\left\langle \delta v_c^{\parallel}(d_b) \right\rangle \equiv \left[ \left\langle \delta_r v_{\parallel}^2 (r = 1.2d_b) \right\rangle \right]^{1/2} = 1.2 C_0^{1/2} (\epsilon/\lambda)^{1/3} d_b^{2/3}. \tag{4.2}$$

Equation (4.2) clearly shows that the approach velocity, instead of following $d_b^{1/3}$ as proposed in the classical framework, scales as $d_b^{2/3}$. The additional 1/3 scaling highlights the missing biased sampling effect that was overlooked before.

Note that the approach velocity refers to the relative velocity between two bubbles at a particular separation scale. In most classical models – and in our work here – it is taken to be the relative velocity at $r = 1.2d_b$, i.e. when the bubbles are nearly in contact. However, an alternative choice is to define it at larger separations, such as at the mean inter-bubble distance determined by the local bubble concentration. In the idealised case where particles move ballistically – with constant velocity magnitude and direction – the relative velocity would be the same regardless of the separation $r$ at which it is measured, and the two definitions would yield identical results. However, this assumption does not hold in turbulent flows, where the relative velocity between bubbles varies with separation $r$, as shown in figure 5. In turbulence, the approach velocity should therefore be interpreted as a weighted average of the relative velocity over a range of separations – from the mean separation (approximately $12d_b$) down to contact. Since this range lies within the inertial subrange, the averaging does not affect the scaling with respect to bubble diameter $d_b$, although it introduces a prefactor. This prefactor depends on a weighting function that reflects the probability that two bubbles remain on a collision course over a given separation $r$. This probability is near one at small separations $r \approx d_b$, and rapidly decays at larger values of $r$, since the likelihood of continued approach over long distances becomes negligible. Consequently, evaluating the approach velocity at $r = 1.2d_b$ provides a good approximation, as the weighting function gives higher importance to bubble pairs that are already close to contact. This makes the choice of selecting relative velocity at $r = 1.2d_b$ both physically reasonable and consistent with prior modelling approaches. Future work is needed to determine the exact correction prefactor introduced by the weighting function, in order to improve quantitative accuracy.



https://doi.org/10.1017/jfm.2025.10603 Published online by Cambridge University Press

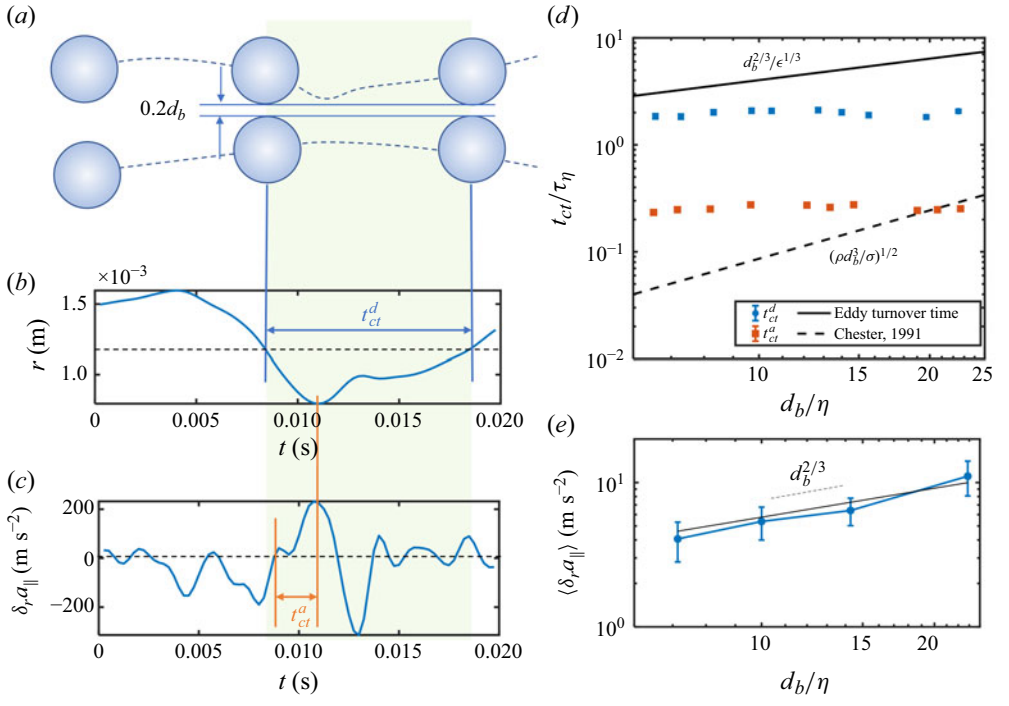


Figure 6. Bubble contact time. (*a*) Schematic of trajectories of a bubble pair through collision, (*b–c*) the time series of the separation between these two bubbles and their relative acceleration along with the extracted contact times $\tau_d$ and $\tau_a$, (*d*) the contact time normalised by the Kolmogorov time scale as a function of the bubble diameter and (*e*) the relative longitudinal acceleration as a function of the bubble diameter.

## 5. Contact time

Once the bubble pairs get sufficiently close and the film begins to drain, the contact time can be calculated based on two different methods, as depicted in figure 6. Figures 6(*a*), 6(*b*) and 6(*c*) show the trajectories, distance $r$ and longitudinal relative acceleration $\delta_r a_\parallel$ of a bubble pair with bubble diameters of 0.44 and 0.46 mm, respectively. One definition of contact time, $t_{ct}^d$, is based on the distance, which measures the duration between bubbles when the gap between the two interfaces falls within $0.2d_b$. Another definition of the contact time, denoted as $t_{ct}^a$, focuses on measuring the duration over which the longitudinal relative acceleration $\delta_r a_\parallel$ becomes positive, indicating a repulsive force between the two bubbles from the lubrication pressure, until $r$ reaches the minimum.

The contact time results based on both the distance ($t_{ct}^d$) and the longitudinal relative acceleration ($t_{ct}^a$) are presented in figure 6(*d*). The contact time determined by either criterion shows no clear trend with the bubble size. These results are clearly different from the prediction either based on the dimensional analysis, i.e. $d_b^{2/3}/\epsilon^{1/3}$, or another relation, $(\rho d_b^3/\sigma)^{1/2}$, where $\rho$ and $\sigma$ are the fluid density and bubble surface tension, derived by Chesters (1991) through the balance between the surface energy and kinetic energy. This difference suggests that larger bubble sizes do not necessarily result in a longer contact time or increased chances for coalescence in turbulence. In the analysis of coalescence efficiency in the following section, $t_{ct}^a$ is adopted as the representative contact time, as it is more directly related to the drainage process.

To explain this difference, an alternative way to estimate the contact time is through $\langle \delta_r v_\parallel \rangle / \langle \delta_r a_\parallel \rangle$, which is the time scale that it takes for the approach velocity to decelerate



https://doi.org/10.1017/jfm.2025.10603 Published online by Cambridge University Press

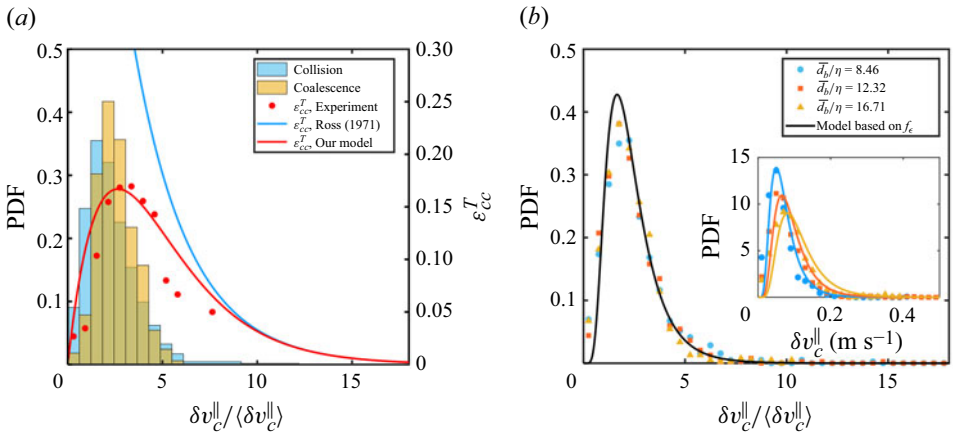


Figure 7. The coalescence efficiency and the PDF of collision velocity. (*a*) The PDF of the coalescence and collision velocity calculated from all collision and coalescence events, along with the ratio in between which is defined as the coalescence efficiency (red symbols). Our model is plotted with a red solid line, to be compared with the one by Coulaloglou (1975) plotted with a blue solid line. (*b*) The PDF of $\delta v_c^{\parallel}$ for different bubble sizes normalised by the velocity scale $\langle \delta v_c^{\parallel} \rangle$ predicted by (4.2). They all collapse and can be modelled based on the log-normal distribution of the turbulence energy dissipation rate $f_\epsilon$ (black solid line).

to zero. With both bubbles tracked simultaneously, the relative acceleration between two bubbles at a given separation can be computed. The separation $r = 1.1d_b$, or film thickness $0.1d_b$, is chosen, which is the midpoint between the start of the film drainage ($r = 1.2d_b$) to the point of contact $r = d_b$. The dependence of $\langle \delta_r a_\parallel (r = 1.2d_b) \rangle$ on bubble size is illustrated in figure 6(*e*). It is evident that $\langle \delta_r a_\parallel \rangle$ scales with $d_b^{2/3}$, suggesting that larger bubble pairs experience stronger repulsive forces. The large repulsive force indicates a high pressure within the film which likely results in local deformation for larger bubbles. With the access to both $\langle \delta_r v_\parallel \rangle$ and $\langle \delta_r a_\parallel \rangle$ experimentally, it is then straightforward to derive the relationship

$$\tau_{ct} \approx \langle \delta_r v_\parallel \rangle / \langle \delta_r a_\parallel \rangle \propto r^{2/3}/r^{2/3} \sim r^0, \tag{5.1}$$

which explains the finding in figure 6(*d*) that the contact time remains nearly constant regardless of the variation in bubble size.

So far, we have measured the critical parameters used in traditional models to predict collision and coalescence. The scaling of the collision velocity and contact time with the bubble size was hypothesised to be $d_b^{1/3}$ and $d_b^{2/3}$, respectively, in traditional models (Coulaloglou 1975; Lee *et al.* 1987; Prince & Blanch 1990*a*; Luo 1995). However, we have shown that these hypotheses are not correct. The corrected scalings should be $d_b^{2/3}$ and $d_b^0$. Such deviation stems from the additional dimensionless number that accounts for the size ratio $d_b/\lambda$ between bubble and turbulence, which measures the effect of biased sampling that was missed in the models.

## 6. Coalescence rate in turbulence

The PDFs of the collision velocity normalised by the model prediction $\langle \delta v_c^{\parallel} \rangle$ in (4.2) for both collision and coalescence events are computed and shown as coloured bars in figure 7(*a*). Although the PDFs appear similar, the peak of the coalescence PDF is shifted towards a higher relative velocity than that of the collision PDF. The bubble coalescence



https://doi.org/10.1017/jfm.2025.10603 Published online by Cambridge University Press

efficiency, $\mathcal{E}_{cc}^{T}$, is calculated by dividing the number of coalescence events ($N_{cc}$, the subscript $cc$ represents 'collision then coalescence') by the number of collision events ($N_c$), i.e. $\mathcal{E}_{cc}^{T} = N_{cc}/N_c$. The value of $\mathcal{E}_{cc}^{T}$ is plotted as red dots in figure 7(*a*) as a function of the collision velocity $\delta v_c^{\parallel}$; $\mathcal{E}_{cc}^{T}(\delta v_c^{\parallel})$ exhibits a peak at an intermediate collision velocity, a Goldilocks zone for coalescence, approaching zero for both small and large collision velocities.

This Goldilocks zone for coalescence efficiency contrasts sharply with the well-adopted traditional model (Coulaloglou 1975; Chesters 1991; Doubliez 1991; Duineveld 1996; Lehr & Mewes 2001; Lehr *et al.* 2002), which is shown as the blue line in figure 7. The traditional model is expressed as $\mathcal{E}_{cc}^{T}(\delta v_c^{\parallel}) = \exp(-t_{dr}/t_{ct})$ (Ross (1971)), where $t_{ct} \approx 1.7$ ms is taken from our experimental result (figure 6*d*) and the drainage time model proposed by Chesters (1975, 1991) and Luo (1995) is adopted:

$$t_{dr} = C_{dr}\rho_c \delta v_c^{\parallel} d_b^2/\sigma, \tag{6.1}$$

where $\rho_c$ represents the density of the carrier fluid and $\sigma$ the surface tension of bubbles. The prefactor $C_{dr}$ is introduced in the model to account for detailed interfacial properties, such as bubble surface mobility, the onset time of the drainage process and surfactant effects. In our study, we tried our best to use reverse osmosis water but the surfactant concentration in the entire tunnel may not be perfectly zero so we determined $C_{dr}$ by fitting the coalescence efficiency model $\mathcal{E}_{cc}^{T}(\delta v_c^{\parallel})$ to our experimental measurements, yielding a value of approximately 7.5. The model prediction is shown as a blue solid line. Although the prediction clearly departs from the measured $\mathcal{E}_{cc}^{T}(\delta v_c^{\parallel})$, the classical model seems to converge with the data at large collision velocities, i.e. $\delta v_c^{\parallel} > 5\langle \delta v_c^{\parallel} \rangle$. At low collision velocities, however, the model predicts nearly 100 % coalescence efficiency yet the data suggest that the coalescence efficiency should continue to decline down to zero.

This mismatch resides in the assumption of the model that the collision velocity is persistent over $t_{dr}$ for the liquid film to be drained. In turbulence, however, the relative velocity between bubbles is affected by the surrounding eddies carrying their own characteristic scales. If the collision velocity is smaller than the eddy velocity, the collision takes too long, longer than the decorrelation time of the flow. In this case, the drainage process is interrupted by the chaotic motion of surrounding eddies in random directions, causing bubble pairs to be driven apart.

As a result, the coalescence efficiency has to account for an additional probability, $\mathcal{P}$, of the bubble collision velocity $\delta v_c^{\parallel}$ being large enough to keep bubble pairs together for coalescence to occur before eddies with velocity scale of $|u_l|$ separate them. If $|u_l| \ll \delta v_c^{\parallel}$, $\mathcal{P}$ should approach one since the eddy velocity is too slow to interrupt coalescence and the process proceeds as if the surrounding flow is frozen. At the opposite limit when $|u_l| \gg \delta v_c^{\parallel}$, $\mathcal{P}$ approaches zero, suggesting that the coalescence cannot happen without sufficient time to drain the film, as is the case for the left tail of curve for $\mathcal{E}_{cc}^{T}$ in figure 7(*a*). Between these two limits, there should exist a critical velocity, $\kappa \delta v_c^{\parallel}$. Then $\mathcal{P}$ can be expressed as

$$\mathcal{P}\left(|u_l| < \kappa \delta v_c^{\parallel}\right) = \int_{-\kappa\delta v_c^{\parallel}}^{\kappa\delta v_c^{\parallel}} f_u(u_l)\mathrm{d}u_l, \tag{6.2}$$

where $f_u(u_l)$ is the PDF of the eddy velocity at the bubble scale which can be approximated by a Gaussian distribution with zero mean and a deviation $C_2(\epsilon d_b)^{2/3}$ since $d_b$ is in the inertial range (Kolmogorov 1949). The final model of $\mathcal{E}_{cc}^{T}$ by including $\mathcal{P}$ and



https://doi.org/10.1017/jfm.2025.10603 Published online by Cambridge University Press

the Ross (1971) model is

$$\mathcal{E}_{cc}^{T}(\delta v_c^{\parallel}) = \mathcal{P}(|u_l| < \kappa \delta v_c^{\parallel}) \exp(-C_{dr}\rho_c \delta v_c^{\parallel} d_b^2/\sigma t_{ct}). \tag{6.3}$$

The model prediction using the mean bubble diameter from experiments $d_b = 12\eta$ is shown as a red curve in figure 7(*a*), which matches well with the experimental results using the fitting parameters $\kappa = 0.14$ constrained mostly by the left tail and $C_{dr} = 7.5$ constrained by the right tail.

Since the coalescence efficiency shows non-trivial dependence on the collision velocity, the PDF of the collision velocity in turbulence becomes important for modeling of coalescence rate, which is also calculated and plotted with symbols in figure 7(*b*) for three different groups of bubble sizes $d_b = 8.46\eta$, $12.32\eta$ and $16.72\eta$. The collision velocities are normalised by their respective mean based on (4.2), $v^* = \delta v_c^{\parallel}/\langle \delta v_c^{\parallel} \rangle$. Since bubbles are transported through eddies across multiple scales, the PDF of the collision velocity can be derived based on the log-normal distribution of the normalised energy dissipation rate $\epsilon^* = \epsilon_r/\langle \epsilon \rangle$ given by (Kolmogorov 1962; Meneveau & Sreenivasan 1987)

$$f_\epsilon(\epsilon^*) = \frac{1}{\epsilon^* \sqrt{2\pi\sigma_{ln\epsilon}^2}} \exp\left[ -\frac{(\ln\epsilon^* - \mu_{ln\epsilon})^2}{2\sigma_{ln\epsilon}^2} \right], \tag{6.4}$$

where $\sigma_{ln\epsilon}^2 = A + \mu \ln(L/r)$ and $\mu_{ln\epsilon} = -\sigma_{ln\epsilon}^2/2$ such that the mean of $\epsilon^*$ given by this distribution is 1. The parameter $\mu = 0.25$ is the intermittency exponent and $A$ is a parameter determined by the specific flow conditions. After normalisation, $v^*$ solely scales with $\epsilon^{*1/3}$, which can be modelled as $v^* = \zeta \epsilon^{*1/3}$, where $\zeta$ is a coefficient that is left out in the non-dimensionalisation. The PDF for $v^*$ can be readily derived as $f_v^c(v^*) = 3v^{*2} f_\epsilon((v^*/\zeta)^3)/\zeta^3$, where $f_\epsilon$ is evaluated at $r = d_b$. We determined both $\zeta$ and $A$ by fitting $f_v^c(v^*)$ to the PDF of $v^*$ from experiments, which are 2.8 and 1, respectively. The model of the PDF of $v^*$ based on (6.4) is plotted as a solid black line in figure 7(*b*), which shows a good agreement with experimental data. We also plotted the dimensional $\delta v_c^{\parallel}$ in the inset of figure 7(*b*) to confirm the agreement between the model and the measured PDF at different sizes.

With the derived PDF of the collision velocity and the coalescence efficiency, the PDF of the coalescence velocity can be formulated as $f_v^{cc}(\delta v_{cc}^{\parallel}) = \mathcal{E}_{cc}^{T}(\delta v_c^{\parallel}) f_v^c(\delta v_c^{\parallel}) / \int_0^\infty \mathcal{E}_{cc}^{T}(\delta v_c^{\parallel}) f_v^c(\delta v_c^{\parallel}) \mathrm{d}\delta v_c^{\parallel}$, where $f_v^c(\delta v_c^{\parallel})$ is the PDF of collision velocity, and $f_v^{cc}(\delta v_{cc}^{\parallel})$ the PDF of collision velocity for coalescing bubble pairs, $\delta v_{cc}^{\parallel}$. Then the average coalescence velocity can be calculated as $\langle \delta v_{cc}^{\parallel} \rangle = \int_0^\infty v f_v^{cc}(v) \mathrm{d}v$. In figure 8(*a*), the model-predicted $\langle \delta v_{cc}^{\parallel} \rangle$ is shown as a red solid line. It is important to note that the calculation of $\mathcal{E}_{cc}^{T}(\delta v_c^{\parallel})$ from (6.3) uses a constant contact time for all bubble sizes, as demonstrated in figure 6. To validate our model prediction, we divided the coalescing bubble pairs into groups with four different sizes, and calculated their mean collision velocity and corresponding 95 % confidence intervals, plotted as scattered squares with error bars.

As shown in figure 8(*a*), our model prediction aligns reasonably with the experimental measurement. Note that symbols represent the statistics of only the coalesced bubbles and the line came from the integration of several quantities, including the new 'Goldilocks effect' of coalescence efficiency, the nearly constant contact time and the PDF of the collision velocity derived from the log-normal distribution of the turbulence energy dissipation rate. For comparison, the prediction by the traditional hypothesised model based on the previous studies (Ross 1971; Chesters 1975; Coulaloglou 1975),



https://doi.org/10.1017/jfm.2025.10603 Published online by Cambridge University Press

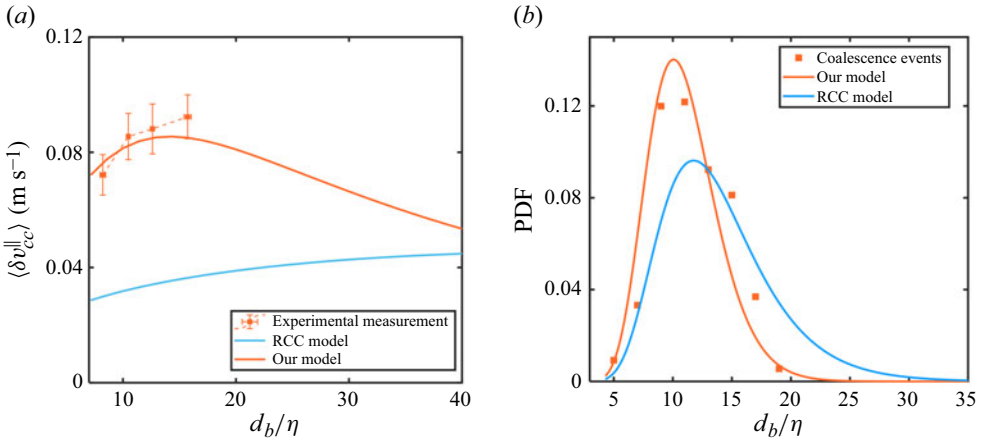


Figure 8. The mean coalescence velocity $\langle|\delta v_{cc}^{\parallel}|\rangle$ and the size distribution of bubble pairs undergoing coalescence. (*a*) The mean $\langle|\delta v_{cc}^{\parallel}|\rangle$ calculated from the coalescence efficiency $\mathcal{E}_{cc}^{T}$ and the PDF of $\delta v_c^{\parallel}$. Predictions by our model and the RCC model (Ross 1971; Chesters 1975; Coulaloglou 1975) are shown for comparison. The experiment measured $\langle|\delta v_{cc}^{\parallel}|\rangle$ is also plotted to validate our model. (*b*) The size distribution of bubble pairs involved in coalescence events predicted by our model and the RCC model.

specifically the RCC model, where $\delta v_c^{\parallel} = [C_2(\epsilon d_b)^{2/3}]^{1/2}$ and $t_{ct} = d_b^{2/3}/(C_2^{1/2}\epsilon^{1/3})$, is also calculated and plotted as a blue solid line. The resulting coalescence velocity is much lower than both our model prediction and experimental measurement because of the lack of bubble–eddy interactions in several key quantities.

Our model can be further validated by calculating the bubble size distribution for bubble pairs involved in coalescence events. The number of coalescence events, $N_{cc}(d_b)$, for the given number of collision events, $N_c(d_b)$, can be estimated as

$$N_{cc}(d_b) = \int_0^\infty N_c(d_b)\mathcal{E}_{cc}^{T}\left(\delta v_c^{\parallel}\right) f_v^c\left(\delta v_c^{\parallel}\right)\mathrm{d}\delta v_c^{\parallel}. \tag{6.5}$$

Since $N_c(d_b)$ is not a function of $\delta v_c^{\parallel}$, it can be factored out of the integral; $N_c(d_b)$ can be presented by the bubble size distribution of collision events $f_d^c(d_b)$ as $N_c(d_b) = N f_d^c(d_b)\mathrm{d}d_b$, where $N$ is the total number of collision events and $f_d^c(d_b)$ is shown as the blue solid line in figure 3(*a*). Defining the integral as $\vartheta(d_b) = \int_0^\infty \mathcal{E}_{cc}^{T}(\delta v_c^{\parallel}) f_v^c(\delta v_c^{\parallel})\mathrm{d}\delta v_c^{\parallel}$, the size distribution of coalescence events can be expressed as $f_d^{cc}(d_b) = f_d^c(d_b)\vartheta(d_b)/\int_0^\infty f_d^c(d_b)\vartheta(d_b)\mathrm{d}d_b$. Since we do not have a model for the size distribution of collision events, we fitted $f_d^c(d_b)$ by a log-normal distribution in figure 3(*a*) with a mean and deviation of 2.6 and 0.12, and focus on the effect of chosen model of $\mathcal{E}_{cc}^{T}$, which can uses either the RCC model (blue line) or the revised Goldilocks zone model (red line in figure 8*b*).

The RCC model clearly deviates from the experimental measurement. Our model shows good agreement with the experimental measurement shown with the red symbols, further demonstrating the validity of our model in predicting coalescence efficiency and collision velocity.

## 7. Discussion

The data analysis and modelling in the previous sections demonstrate that turbulence significantly influences bubble coalescence through four key mechanisms: clustering,



https://doi.org/10.1017/jfm.2025.10603 Published online by Cambridge University Press

| Quantities | RCC models | Our models | Eq number |
|---|---|---|---|
| Collision velocity $\delta v_c^{\parallel}$ | $(\epsilon d_b)^{1/3}$ | $1.2C_0^{1/2}(\epsilon/\lambda)^{1/3}d_b^{2/3}$ | (4.2) |
| Contact time $t_{ct}$ | $d_b^{2/3}/\epsilon^{1/3}$ | $d_b^0$ | (5.1) |
| Coalescence efficiency $\mathcal{E}_{cc}^T$ | $\exp(-t_{dr}/t_{ct})$ | $\mathcal{P}(u_l < \kappa\delta v_c^{\parallel})\exp(-t_{dr}/t_{ct})$ | (6.3) |

Table 1. Comparison between the RCC models and our models.

biased sampling, constant contact time and eddy-driven separation. These mechanisms, highlighted in orange in figure 1, collectively shape the coalescence dynamics by modifying collision rates and coalescence efficiency. The comparison between the traditional models (RCC models) and our models is summarised in table 1.

The biased sampling effect enhances bubble collisions by increasing the collision frequency for larger bubbles. Since larger bubbles extract more energy from their corresponding bubble-sized eddies, their collision velocity scales with a larger exponent to the bubble size than previously expected, which results in a higher collision frequency as bubble size increases.

Another key is the clustering effect, which increases the local concentration of similar-sized bubbles with the Stokes number $St_{d_b}$ close to 1, leading to preferential interactions among bubbles within a specific size range dictated by the background turbulence. In contrast to biased sampling, clustering does not favour the smallest or largest bubbles, but instead creates an optimal size range for bubble collisions. In our study, we computed $g_{CL}$ in (3.1) to represent the clustering effect shown in figure 3(*b*).

After two bubbles collide, the observed contact time between them is completely different from the commonly believed bubble-sized eddy turnover time. This discrepancy suggests that the bubble contact time is less dependent on surrounding turbulent vortices and instead more influenced by bubble–bubble interaction. In comparison with the eddy turnover time, the model by Chesters (1991) provides a better order of magnitude estimation as their model focused on the time scale of the energy transfer from the bubble kinetic energy to the bubble surface energy. But their predicted scaling with bubble size still fails to match the experimental results. Our results indicate that the deceleration during the collision exhibits almost the same scaling with bubble size as the bubble collision velocity. As a result, the contact time shows little dependence on the bubble size since the contact time scales with the ratio between relative velocity and deceleration.

In addition to the contact time, turbulence brings in another key mechanism that alters the coalescence efficiency – the eddy-driven bubble separation. As a result, coalescence efficiency is peaked within an optimal collision velocity range, creating a 'Goldilocks' zone where coalescence occurs when collision velocities are neither too fast nor too slow.

It is important to acknowledge that, apart from the turbulence effect, the interfacial property also can significantly modify the coalescence efficiency. For example, adding surfactants to the carrier flow can further reduce the bubble coalescence rate (Takagi & Matsumoto 2011). Surfactants lower the surface tension $\sigma$, which increases the drainage time and, consequently, decreases the coalescence efficiency, as described by (6.3). Additionally, surfactants affect bubble surface mobility, further prolonging the drainage time. Both effects can be incorporated into our model by adjusting $C_{dr}$ and $\sigma$. If the surfactant concentration gradient exists on the bubble's surface, the Marangoni effect becomes significant. This effect resists film thinning and increases the drainage time. The extent of this resistance depends on the surfactant concentration gradient and the film

https://doi.org/10.1017/jfm.2025.10603 Published online by Cambridge University Press

thickness (Oolman & Blanch 1986; Prince & Blanch 1990*a*), introducing a more complex influence than surface tension alone, which requires further investigation.

Similar to surfactants, dissolved salts significantly impact bubble coalescence through distinct physicochemical mechanisms (Martínez-Mercado *et al.* 2007). Beyond a critical salt concentration, electrolytes inhibit coalescence, stabilising foam (Craig, Ninham & Pashley 1993; Weissenborn & Pugh 1996; Firouzi *et al.* 2015). Proposed mechanisms include (i) electrostatic repulsion from ion-specific adsorption (Duignan 2021), (ii) Gibbs–Marangoni stresses resisting film thinning (Henry *et al.* 2007; Yaminsky *et al.* 2010), (iii) hydrophobic interactions preventing film rupture (Yaminsky & Ninham 1993) and (iv) interfacial viscosity effects slowing drainage (Marrucci 1969; Prince & Blanch 1990*a*; Weissenborn & Pugh 1996). While these mechanisms explain key observations, they fail to predict the sharp transition at the critical salt concentration (Lessard & Zieminski 1971) or its dependence on the collision velocity, as observed in dynamic coalescence experiments (Li *et al.* 2025). The complex role of salts in bubble coalescence remains poorly understood, making quantitative modelling challenging.

Nevertheless, for simplified interfacial properties, with all turbulence effects included, the bubble coalescence rate between bubble pair with size $d_b$ can be expressed as

$$\dot{n}(d_b) = \int_0^\infty 4n^2 f_d^c(d_b)\mathrm{d}d_b \pi d_b^2 \delta v_c^{\parallel} \mathcal{E}_{cc}^T\left(\delta v_c^{\parallel}\right) f_v^c\left(\delta v_c^{\parallel}\right)\mathrm{d}\delta v_c^{\parallel}, \tag{7.1}$$

which completes the modelling of bubble coalescence in turbulence. From a simulation perspective, the coalescence rate at time $t$ is determined by taking inputs, such as the instantaneous bubble size distribution (III) and turbulence characteristics (I), and interfacial properties such as surface tension (II.1) and ion concentration (II.2). The new effects of turbulence discovered in our study, such as the clustering effect (I.1), biased sampling (I.2), constant contact time (I.3) and eddy-driven bubble separation (I.4) during time $\Delta t$, govern the bubble coalescence dynamics in turbulence. Once the coalescence rate $\dot{n}$ (IV) is obtained, it is incorporated into the population balance equation, updating the bubble size distribution from time $t$ to $t + \Delta t$. This iterative process allows for the continuous evolution of the bubble population, providing insights into the statistical dynamics of coalescence in turbulent flows.

## 8. Conclusion

In this study, with the new breakthrough in experimental methods, for the first time, we measured the collision and coalescence dynamics of bubbles in turbulence in three dimensions, covering both the collision and coalescence rates as well as the key statistics that govern these processes. The classical models that have been widely adopted often assume that bubble motion mirrors the surrounding eddies. The experimental data show that the classical model misses several key quantities, as it fails to consider the biased sampling of bubbles in eddies of comparable sizes and the eddy-induced separation effect on bubble coalescence. By incorporating these factors, we successfully developed new scalings for the bubble velocity and the coalescence efficiency model. Turbulence influences the bubble dynamics in two opposing ways: it enhances collision for larger bubbles through high-energy eddies of comparable size, while simultaneously inhibiting coalescence by separating bubble pairs via surrounding eddies. As a result, it produces a Goldilocks zone for bubble coalescence with both large and small collision velocities resulting in low coalescence efficiency.

**Funding.** We acknowledge the financial support from the National Science Foundation under the award number CAREER-1905103. This project was also partially supported by the ONR award: N00014-21-1-2083.



https://doi.org/10.1017/jfm.2025.10603 Published online by Cambridge University Press

**Declaration of interests.** The authors report no conflict of interest.

**Data availability statement.** All the data supporting this work are available from the corresponding author upon reasonable request. The bubble-tracking code used for 3-D bubble tracking is available at https://github.com/JHU-NI-LAB/OpenLPTGUI. Other codes for image processing and analyses that are reported in the paper are available from the corresponding author upon request.

## Appendix A. Homogeneous isotropic turbulence

The turbulence is generated within an octagonal test section 23 cm in size (the diameter of the inscribed circle) and 80 cm in height. As shown in figure 2(*b*), the jet array consists of 88 jet nozzles with a diameter of 5 mm that are connected to the side openings via internal channels, and with 52 square through holes allowing co-flow from the tunnel top into the test section. In the experiments, 22 jets spaced uniformly at 4.2 cm apart were actively shooting downward. The jet velocity at the nozzle is 5.1 m s$^{-1}$, complemented by a co-flow velocity of 0.23 m s$^{-1}$, resulting in a mean flow velocity of 0.1 m s$^{-1}$ in the test section. The cameras were positioned 23 cm downstream from the jet array, providing sufficient distance for the jet flow to develop fully into homogeneous isotropic turbulence (Tan *et al.* 2023*a*). The view volume of all cameras was approximately 60 × 60 × 40 mm$^3$, centred within the test section. Bubbles generated by a bubble generator at the bottom of the test section are sized from 0.4 to 2 mm in diameter, with a void fraction of around 0.04 %. The rise velocity of generated bubbles is approximately 0.1 m s$^{-1}$ (Salibindla *et al.* 2020), counteracted by the mean flow in the test section to increase the residence time.

## Appendix B. Three-dimensional measurements

In the experiments, the shadows of bubbles were projected onto all four cameras using backlit LED panels. The bubbles were then reconstructed and tracked using our in-house bubble-tracking algorithm (Tan *et al.* 2023*b*). This algorithm employs a similar tracking framework to our OpenLPT code (Tan *et al.* 2019, 2020) but accounts for the finite size of bubble images, leveraging both temporal and spatial information from bubble images, which enables it to handle densely packed bubble images with overlap. Image cross-correlation was used to accurately determine the 3-D bubble locations, achieving sub-pixel precision through bilinear interpolation of the correlation. The resulting trajectories were smoothed by convolution with a Gaussian kernel (Mordant *et al.* 2004; Ni *et al.* 2012). The filter size was carefully chosen to preserve velocity and acceleration data while effectively eliminating noise.

## References


Bartlett, C., Oratis, A.T., Santin, M. & Bird, J.C. 2023 Universal non-monotonic drainage in large bare viscous bubbles. *Nat. Commun.* **14** (1), 877.

Calzavarini, E., Van den, B., Thomas, H., Toschi, F. & Lohse, D. 2008 Quantifying microbubble clustering in turbulent flow from single-point measurements. *Phys. Fluids* **20** (4), 040702.

Chen, J.-D., Hahn, P.S. & Slattery, J.C. 1984 Coalescence time for a small drop or bubble at a fluid-fluid interface. *AIChE J.* **30** (4), 622–630.

Chesters, A_K. 1991 Modelling of coalescence processes in fluid-liquid dispersions: a review of current understanding. *Chem. Engng Res. Design* **69** (A4), 259–270.

Chesters, A.K. & Hofman, G. 1982 Bubble coalescence in pure liquids. In Mechanics and Physics of Bubbles in Liquids: Proceedings IUTAM Symposium, held in Pasadena, California, 15-19 June 1981, pp. 353–361. Springer.

Chesters, A.K. 1975 The applicability of dynamic-similarity criteria to isothermal, liquid-gas, two-phase flows without mass transfer. *Intl J. Multiphase Flow* **2** (2), 191–212.




https://doi.org/10.1017/jfm.2025.10603 Published online by Cambridge University Press

CHESTERS, A.K. & BAZHLEKOV, I.B. 2000 Effect of insoluble surfactants on drainage and rupture of a film between drops interacting under a constant force. *J. Colloid Interface Sci.* **230** (2), 229–243.
COULALOGLOU, C.A. & TAVLARIDES, L.L. 1977 Description of interaction processes in agitated liquid-liquid dispersions. *Chem. Engng Sci.* **32** (11), 1289–1297.
COULALOGLOU, C.A. 1975 *Dispersed Phase Interactions in an Agitated Flow Vessel*. Illinois Institute of Technology.
CRAIG, V.S.J., NINHAM, B.W. & PASHLEY, R.M. 1993 Effect of electrolytes on bubble coalescence. *Nature* **364** (6435), 317–319.
DANOV, K.D., VALKOVSKA, D.S. & IVANOV, I.B. 1999 Effect of surfactants on the film drainage. *J. Colloid Interface Sci.* **211** (2), 291–303.
DAS, S.K. 2015 Development of a coalescence model due to turbulence for the population balance equation. *Chem. Engng Sci.* **137**, 22–30.
DOUBLIEZ, L. 1991 The drainage and rupture of a non-foaming liquid film formed upon bubble impact with a free surface. *Intl J. Multiphase Flow* **17** (6), 783–803.
DUIGNAN, T.T. 2021 The surface potential explains ion specific bubble coalescence inhibition. *J. Colloid Interface Sci.* **600**, 338–343.
DUINEVELD, P.C. 1996 Bouncing and coalescence of two bubbles in water. PhD dissertation, University of Twente.
FIROUZI, M., HOWES, T. & NGUYEN, A.V. 2015 A quantitative review of the transition salt concentration for inhibiting bubble coalescence. *Adv. Colloid Interface Sci.* **222**, 305–318.
GONG, S., GAO, N., HAN, L. & LUO, H. 2020 A theoretical model for bubble coalescence by coupling film drainage with approach processes. *Chem. Engng Sci.* **213**, 115387.
HENRY, C.L., DALTON, C.N., SCRUTON, L. & CRAIG, V.S.J. 2007 Ion-specific coalescence of bubbles in mixed electrolyte solutions. *J. Phys. Chem. C* **111** (2), 1015–1023.
HUANG, G., HESSENKEMPER, H., TAN, S., NI, R., SOMMER, A., BRAGG, A.D. & MA, T., 2025 Taylor dispersion of bubble swarms rising in quiescent liquid. *J. Fluid Mech.* **1014**, R1.
JEELANI, S.A.K. & HARTLAND, S. 1998 Effect of surface mobility on collision of spherical drops. *J. Colloid Interface Sci.* **206** (1), 83–93.
KAMP, A.M., CHESTERS, A.K., COLIN, C. & FABRE, J. 2001 Bubble coalescence in turbulent flows: a mechanistic model for turbulence-induced coalescence applied to microgravity bubbly pipe flow. *Intl J. Multiphase Flow* **27** (8), 1363–1396.
KATZ, J. & SHENG, J. 2010 Applications of holography in fluid mechanics and particle dynamics. *Annu. Rev. Fluid Mech.* **42** (1), 531–555.
KENNARD, E.H. *et al.* 1938 *Kinetic Theory of Gases*, vol. 483. McGraw-Hill New York.
KOLMOGOROV, A. 1949 On the breakage of drops in a turbulent flow. *Dokl. Akad. Navk. SSSR* **66**, 825–828.
KOLMOGOROV, A.N. 1962 A refinement of previous hypotheses concerning the local structure of turbulence in a viscous incompressible fluid at high Reynolds number. *J. Fluid Mech.* **13** (1), 82–85.
LEBON, B., PERRET, G., COËTMELLEC, S., GODARD, G., GRÉHAN, G., LEBRUN, D. & BROSSARD, J. 2016 A digital holography set-up for 3D vortex flow dynamics. *Exp. Fluids* **57** (6), 1–11.
LEE, C.-H., ERICKSON, L.E. & GLASGOW, L.A. 1987 Bubble breakup and coalescence in turbulent gas–liquid dispersions. *Chem. Engng Commun.* **59** (1–6), 65–84.
LEHR, F. & MEWES, D. 2001 A transport equation for the interfacial area density applied to bubble columns. *Chem. Engng Sci.* **56** (3), 1159–1166.
LEHR, F., MILLIES, M. & MEWES, D. 2002 Bubble-size distributions and flow fields in bubble columns. *AIChE J.* **48** (11), 2426–2443.
LESSARD, R.R. & ZIEMINSKI, S.A. 1971 Bubble coalescence and gas transfer in aqueous electrolytic solutions. *Ind. Engng Chem. Fund.* **10** (2), 260–269.
LI, D., MANICA, R., CHEN, Z., WANG, S., LIU, Q. & ZHANG, H. 2025 Bubble coalescence principle in saline water. *Proc. Natl Acad. Sci.* **122** (5), e2417043122.
LIAO, Y. & LUCAS, D. 2010 A literature review on mechanisms and models for the coalescence process of fluid particles. *Chem. Engng Sci.* **65** (10), 2851–2864.
LOHSE, D. 2018 Bubble puzzles: from fundamentals to applications. *Phys. Rev. Fluids* **3** (11), 110504.
LOTH, E. 2000 Numerical approaches for motion of dispersed particles, droplets and bubbles. *Prog. Energ. Combust.* **26** (3), 161–223.
LU, J., CORVALAN, C.M., CHEW, Y.M.J. & HUANG, J.-Y. 2019 Coalescence of small bubbles with surfactants. *Chem. Engng Sci.* **196**, 493–500.
LUO, H. 1995 Coalescence, breakup and liquid circulation in bubble column reactors. *PhD thesis*, University of Trondheim.



https://doi.org/10.1017/jfm.2025.10603 Published online by Cambridge University Press

MA, T., TAN, S., NI, R., HESSENKEMPER, H. & BRAGG, A.D. 2025 Kolmogorov scaling in bubble-induced turbulence. *Phys. Rev. Lett.* **134** (24), 244001.

MARRUCCI, G. 1969 A theory of coalescence. *Chem. Engng Sci.* **24** (6), 975–985.

MARTÍNEZ-MERCADO, J., PALACIOS-MORALES, C.A. & ZENIT, R. 2007 Measurement of pseudoturbulence intensity in monodispersed bubbly liquids for $10 < \mathrm{Re} < 500$. *Phys. Fluids* **19** (10), 103302.

MASUK, A.U.M., SALIBINDLA, A. & NI, R. 2019*a* A robust virtual-camera 3D shape reconstruction of deforming bubbles/droplets with additional physical constraints. *Intl J. Multiphase Flow* **120**, 103088.

MASUK, A.U.M., SALIBINDLA, A., TAN, S. & NI, R. 2019*b* V-onset (vertical octagonal noncorrosive stirred energetic turbulence): a vertical water tunnel with a large energy dissipation rate to study bubble/droplet deformation and breakup in strong turbulence. *Rev. Sci. Instrum.* **90** (8), 085105.

MATHAI, V., CALZAVARINI, E., BRONS, J., SUN, C. & LOHSE, D. 2016 Microbubbles and microparticles are not faithful tracers of turbulent acceleration. *Phys. Rev. Lett.* **117** (2), 024501.

MATHAI, V., HUISMAN, S.G., SUN, C., LOHSE, D. & BOURGOIN, M. 2018 Dispersion of air bubbles in isotropic turbulence. *Phys. Rev. Lett.* **121** (5), 054501.

MATHAI, V., LOHSE, D. & SUN, C. 2020 Bubbly and Buoyant particle–Laden turbulent flows. *Annu. Rev. Conden. Matter Phys.* **11** (1), 529–559.

MENEVEAU, C. & SREENIVASAN, K.R. 1987 The multifractal spectrum of the dissipation field in turbulent flows. *Nuclear Phys. B - Proc. Supplements* **2**, 49–76.

MORDANT, N., CRAWFORD, A.M. & BODENSCHATZ, E. 2004 Experimental Lagrangian acceleration probability density function measurement. *Physica D: Nonlinear Phenom.* **193** (1–4), 245–251.

NI, R. 2024 Deformation and breakup of bubbles and drops in turbulence. *Annu. Rev. Fluid Mech.* **56** (1), 319–347.

NI, R., HUANG, S.-D. & XIA, K.-Q. 2012 Lagrangian acceleration measurements in convective thermal turbulence. *J. Fluid Mech.* **692**, 395–419.

OOLMAN, T. & BLANCH, H. 1986 Bubble coalescence in stagnant liquids. *Chem. Engng Commun.* **43** (4–6), 237–261.

OZAN, S.C., HOSEN, H.F. & JAKOBSEN, H.A. 2021 On the prediction of coalescence and rebound of fluid particles: a film drainage study. *Intl J. Multiphase Flow* **135**, 103521.

OZAN, S.C., SOLSVIK, J. & JAKOBSEN, H.A. 2023 A bubble coalescence kernel combining the characteristics of the film drainage, energy, and critical velocity models. *Chem. Engng Sci.* **269**, 118458.

PAULSEN, J.D., CARMIGNIANI, R., KANNAN, A., BURTON, J.C. & NAGEL, S.R. 2014 Coalescence of bubbles and drops in an outer fluid. *Nat. Commun.* **5** (1), 1–7.

PRESS, W.H., TEUKOLSKY, S.A., VETTERLING, W.T. & FLANNERY, B.P. 2007 *Numerical Recipes 3rd Edition: The Art of Scientific Computing*. Cambridge University Press.

PRINCE, M.J. & BLANCH, H.W. 1990*a* Bubble coalescence and break-up in air-sparged bubble columns. *AIChE J.* **36** (10), 1485–1499.

PRINCE, M.J. & BLANCH, H.W. 1990*b* Transition electrolyte concentrations for bubble coalescence. *Aiche J.* **36** (9), 1425–1429.

PUMIR, A. & WILKINSON, M. 2016 Collisional aggregation due to turbulence. *Annu. Rev. Conden. Matter Phys.* **7**, 141–170.

QI, Y., TAN, S., CORBITT, N., URBANIK, C., SALIBINDLA, A.K.R. & NI, R. 2022 Fragmentation in turbulence by small eddies. *Nat. Commun.* **13** (1), 1–8.

QI, Y., XU, X., TAN, S., ZHONG, S., WU, Q. & NI, R. 2024 Breaking bubbles across multiple time scales in turbulence. *J. Fluid Mech.* **983**, A24.

RENSEN, J., LUTHER, S. & LOHSE, D. 2005 The effect of bubbles on developed turbulence. *J. Fluid Mech.* **538**, 153–187.

ROSS, S.L. 1971 *Measurements and Models of the Dispersed Phase Mixing Process*. University of Michigan.

SALIBINDLA, A.K.R., MASUK, A.U.M., TAN, S. & NI, R. 2020 Lift and drag coefficients of deformable bubbles in intense turbulence determined from bubble rise velocity. *J. Fluid Mech.* **894**, A20.

SHAO, S., MALLERY, K., KUMAR, S.S. & HONG, J. 2020 Machine learning holography for 3D particle field imaging. *Opt. Express* **28** (3), 2987–2999.

SHNAPP, R., BRIZZOLARA, S., NEAMTU-HALIC, M.M., GAMBINO, A. & HOLZNER, M. 2023 Universal alignment in turbulent pair dispersion. *Nat. Commun.* **14** (1), 4195.

SONG, Y., QIAN, Y., ZHANG, T., YIN, J. & WANG, D. 2022 Simultaneous measurements of bubble deformation and breakup with surrounding liquid-phase flow. *Exp. Fluids* **63** (5), 1–20.

TAKAGI, S. & MATSUMOTO, Y. 2011 Surfactant effects on bubble motion and bubbly flows. *Annu. Rev. Fluid Mech.* **43** (1), 615–636.

TAN, S. & NI, R. 2022 Universality and intermittency of pair dispersion in turbulence. *Phys. Rev. Lett.* **128** (11), 114502.

https://doi.org/10.1017/jfm.2025.10603 Published online by Cambridge University Press

TAN, S., SALIBINDLA, A., MASUK, A.U.M. & NI, R. 2019 An open-source shake-the-box method and its performance evaluation. In 13th international symposium on particle image velocimetry.

TAN, S., SALIBINDLA, A., MASUK, A.U.M. & NI, R. 2020 Introducing OpenLPT: new method of removing ghost particles and high-concentration particle shadow tracking. *Exp. Fluids* **61** (2), 1–16.

TAN, S., XU, X., QI, Y. & NI, R. 2023*a* Scalings and decay of homogeneous, nearly isotropic turbulence behind a jet array. *Phys. Rev. Fluids* **8** (2), 024603.

TAN, S., ZHONG, S. & NI, R. 2023*b* 3D Lagrangian tracking of polydispersed bubbles at high image densities. *Exp. Fluids* **64** (4), 85.

TOSCHI, F. & BODENSCHATZ, E. 2009 Lagrangian properties of particles in turbulence. *Annu. Rev. Fluid Mech.* **41**, 375–404.

VELA-MARTÍN, A. & AVILA, M. 2022 Memoryless drop breakup in turbulence. *Sci. Adv.* **8** (50), eabp9561.

WANG, T., WANG, J. & JIN, Y. 2005 Population balance model for gas–liquid flows: influence of bubble coalescence and breakup models. *Indust. Engng Chem. Res.* **44** (19), 7540–7549.

WANG, Z., DE, W., XANDER, M. & TOSCHI, F. 2024 Localization–delocalization transition for light particles in turbulence. *Proc. Natl Acad. Sci.* **121** (38), e2405459121.

WEISSENBORN, P.K. & PUGH, R.J. 1996 Surface tension of aqueous solutions of electrolytes: relationship with ion hydration, oxygen solubility, and bubble coalescence. *J. Colloid Interface Sci.* **184** (2), 550–563.

WILLIAMS, F.A. 1985 Turbulent combustion. In *the Mathematics of Combustion*, pp. 97–131. SIAM.

WU, Q., KIM, S., ISHII, M. & BEUS, S.G. 1998 One-group interfacial area transport in vertical bubbly flow. *Intl J. Heat Mass Transfer* **41** (8–9), 1103–1112.

WU, Y., ZHANG, H., WU, X. & CEN, K. 2020 Quantifying bubble size and 3D velocity in a vortex with digital holographic particle tracking velocimetry (DHPTV). *Flow Meas. Instrum.* **76**, 101826.

XUE, T., QU, L. & WU, B. 2013 Matching and 3-D reconstruction of multibubbles based on virtual stereo vision. *IEEE Trans. Instrum. Meas.* **63** (6), 1639–1647.

YAMINSKY, V.V. & NINHAM, B.W. 1993 Hydrophobic force: lateral enhancement of subcritical fluctuations. *Langmuir* **9** (12), 3618–3624.

YAMINSKY, V.V., OHNISHI, S., VOGLER, E.A. & HORN, R.G. 2010 Stability of aqueous films between bubbles. Part 1. the effect of speed on bubble coalescence in purified water and simple electrolyte solutions. *Langmuir* **26** (11), 8061–8074.

ZHAO, K., POMES, F., VOWINCKEL, B., HSU, T.-J., BAI, B. & MEIBURG, E. 2021 Flocculation of suspended cohesive particles in homogeneous isotropic turbulence. *J. Fluid Mech.* **921**, A17.

https://doi.org/10.1017/jfm.2025.10603 Published online by Cambridge University Press